

Was SNR 0509-67.5 the result of a double detonation?

SOHAM MANDAL,^{1,2} PARVIZ GHAVAMIAN,³ PRIYAM DAS,⁴ IVO ROLF SEITENZAHL,⁵ SHAZRENE MOHAMED,^{1,2,6,7,8} AND
ASHLEY J. RUITER⁴

¹*Department of Astronomy, University of Virginia, 530 McCormick Road, Charlottesville, VA 22904, USA*

²*Virginia Institute for Theoretical Astronomy, University of Virginia, Charlottesville, VA 22904, USA*

³*Department of Physics, Astronomy and Geosciences, Towson University, Towson, MD, 21252; pghavamian@towson.edu*

⁴*School of Science, The University of New South Wales, Australian Defence Force Academy, Northcott Drive, Campbell, Canberra, ACT 2600, Australia*

⁵*Mathematical Sciences Institute, Australian National University, Canberra, ACT 0200, Australia*

⁶*South African Astronomical Observatory, P.O Box 9, Observatory, 7935, Cape Town, South Africa*

⁷*Department of Astronomy, University of Cape Town, Private Bag X3, Rondebosch, 7701, Cape Town, South Africa*

⁸*NITheCS National Institute for Theoretical and Computational Sciences, South Africa*

ABSTRACT

Type Ia supernovae (SNe) occur when a white dwarf (WD) is disrupted by runaway thermonuclear burning. The nature and observable signatures of the mechanism triggering the explosion are still debated. In this work, we study how supernova remnants (SNRs) are impacted by the ‘double detonation’ explosion mechanism, or a helium shell detonation in a sub-Chandrasekhar WD followed by a core detonation. We evolve double detonation SN models to the remnant phase (up to several centuries) and measure the size of substructures formed in the SNR as a result of turbulent activity. We compare our results to small-scale substructures seen in high-resolution optical observations of the SNR 0509-67.5. Substructures dominated by iron in that SNR are observed to be about 40% larger than those dominated by sulfur. This has been shown to be a definitive signature of the explosion of a sub-Chandrasekhar WD by Mandal et al. Comparisons against our suite of SNR models with a range of core and shell masses suggest that the specific substructure sizes in SNR 0509-67.5 are most consistent with the double detonation explosion of a WD with a carbon-oxygen core mass and a helium shell mass of $1M_{\odot}$ and $> 0.05M_{\odot}$, respectively.

Keywords: hydrodynamics — shock waves — supernova remnants — hydrodynamic instabilities — thermonuclear supernovae

1. INTRODUCTION

Type Ia supernovae (SNe Type Ia) are runaway thermonuclear explosions of white dwarf (WD) stars assumed to be rich in carbon and oxygen. They constitute an important pathway to the formation of elements in the present-day universe (and are the dominant source of iron-group elements; see Maoz & Graur 2017). They are regarded as crucial distance indicators in the cosmological distance ladder (Kirshner 2010), owing to their famous characteristic of having absolute luminosities that are tightly correlated with the width of their lightcurves

(Phillips 1993; Phillips & Burns 2017)¹. This is partly the reason why Type Ia SNe have been traditionally regarded as members of a homogenous population. Conventionally, Type Ia SNe were thought to occur when a carbon oxygen WD approaches the Chandrasekhar mass limit (M_{ch} ; Chandrasekhar 1931) via accretion. The near-Chandrasekhar mass (near- M_{ch} henceforth) WD becomes degenerate and thus cannot cool adiabatically in response to continued mass accretion. As a result its central density and temperature increases dramatically, leading to runaway nuclear burning and explosion of the WD (Ruiter & Seitenzahl 2025).

soham@virginia.edu

¹ albeit more modern studies find that $\sim 30\%$ of SNe Type Ia do not follow this correlation (Taubenberger 2017).

Early models considered the expanding nuclear flame front to be either strictly subsonic or strictly supersonic; called deflagration (Nomoto et al. 1984; Iwamoto et al. 1999) and detonation (Arnett 1969; Hansen & Wheeler 1969), respectively. Pure detonation models exhibited very high explosion energies and production of predominantly iron-group elements (IGEs), both of which are in conflict with observations (Arnett et al. 1971). The deflagration models, on the other hand, suffered from low ejecta kinetic energy and production of lower ^{56}Ni than is required to explain normal Type Ia SNe (Niemeyer et al. 1996; Niemeyer & Woosley 1997). The “delayed detonation” class of models were proposed to address this issue. In these models, nuclear burning initiates near the center of a near- M_{ch} WD as a subsonic flame. It later transitions to develop a supersonic combustion front, or detonation (Ivanova et al. 1974; Khokhlov 1991a,b). A popular example of this class is the deflagration-to-detonation transition model (DDT; see review by Röpke 2017).

Despite the success of these models, the idea of near- M_{ch} WDs being progenitors of Type Ia SNe were found to suffer from two major issues: they are less abundant in nature compared to their sub- M_{ch} counterparts (Kepler et al. 2007; Torres et al. 2021), and stable growth of WD masses to near- M_{ch} values requires rather finely-tuned accretion (Nomoto et al. 2007). This led to the suggestion that sub- M_{ch} WDs could also give rise to Type Ia SNe. This is called the double detonation (DD) model, in which a near-surface detonation occurs in the accreted helium shell of a sub- M_{ch} WD. This detonation sends a shockwave into the core of the WD, causing a second detonation and a subsequent thermonuclear runaway (Livne 1990; Woosley & Weaver 1994; Fink et al. 2007, 2010; Shen & Bildsten 2014; Polin et al. 2019). Another possible channel for Type Ia SNe from sub- M_{ch} WDs is the violent merger of two sub- M_{ch} WDs, followed by carbon ignition near the core of one of the WDs (Pakmor et al. 2010, 2012).

Both near- M_{ch} and sub- M_{ch} WD progenitors are now thought to be needed to explain the range of specific properties of observed Type Ia SNe, such as ejecta mass derived from lightcurve modeling (Scalzo et al. 2014; Bora et al. 2024), Mn/Fe ratio (Seitenzahl et al. 2013; Lach et al. 2020), nebular spectra-inferred Fe/Ni ratio (Flörs et al. 2020) and lightcurve-inferred $^{57}\text{Ni}/^{56}\text{Ni}$ ratio (Seitenzahl et al. 2009; Röpke et al. 2012; Tiwari et al. 2022), with most of the proposed explosion mechanisms likely at play. Perhaps then, it is not surprising that we have moved from the ‘homogenous family of lightcurves’ paradigm to a much more diverse family of Type Ia lightcurves and spectra (Taubenberger

2017; Gal-Yam 2017), especially with the advent of modern high-cadence surveys such as the Palomar Transient Factory (PTF; Law et al. 2009), the All-Sky Automated Survey for SuperNovae (ASAS-SN; Kochanek et al. 2017), the Zwicky Transient Facility (ZTF) Bright Transient Survey (Perley et al. 2020), the Young Supernova Experiment (YSE; Aleo et al. 2023), the Dark Energy Survey (DES Collaboration et al. 2024), and the upcoming Legacy Survey of Space and Time (LSST; Ivezić et al. 2019). However, no clear correspondence between observed properties of Type Ia SNe spectra or lightcurves and the proposed thermonuclear explosion mechanisms has been discovered yet (Hillebrandt et al. 2013; Ruiter & Seitenzahl 2025).

Some studies have approached this problem from a different direction, that is, studying remnants of Type Ia SNe to identify the signatures of the mechanism responsible for the explosion (Badenes et al. 2006; Seitenzahl et al. 2019; Ferrand et al. 2021; Mandal et al. 2025). A specific example of such a signature is the presence of a large-scale conical ‘shadow’ in the ejecta of a Type-Ia SNR that exploded via the DD channel in the presence of another WD (Ferrand et al. 2022). An ideal candidate for this line of investigation is the well-studied supernova remnant (SNR) 0509-67.5, located in the Large Magellanic Cloud (LMC). SNR 0509-67.5 (henceforth 0509) has been observed extensively in radio (Bozzetto et al. 2014), infrared (Seok et al. 2013), optical (Helder et al. 2010; Hovey et al. 2015), UV (Ghavamian et al. 2007) and X-ray bands (Warren & Hughes 2004; Kosenko et al. 2008). The light echo spectrum of 0509 suggests that it belongs to the class of overluminous, slowly fading, 1991T-like SNe (Rest et al. 2008). 1D hydrodynamic models with detailed non-equilibrium ionization calculations (Badenes et al. 2008) also support this conclusion, showing that both the dynamics and the X-ray line flux ratios for 0509 are most consistent with a highly energetic and luminous SN akin to SN 1991T (Phillips et al. 2022, 2024). Hydrodynamics-based Bayesian analysis of the kinematics of 0509 as revealed by the Hubble Space Telescope (Arunachalam et al. 2022) suggest a large value of explosion energy ($\sim 1.3 \times 10^{51}$ erg), again favoring a 1991T spectral subtype for this Type Ia SNR.

In addition to spectral classification, Badenes et al. (2008) also show that 1D delayed detonation (DDT) explosion of near- M_{ch} WDs are a good match for 0509. On the other hand, Seitenzahl et al. (2019) argue in favor of a sub- M_{ch} WD explosion. They obtain high-resolution optical observations that reveal highly ionized Fe clumps in 0509. Using detailed time-dependent ionization balance calculations based on analytic SNR models (Truelove & McKee 1999), they find that the dynamics and

strongly ionized state of the Fe clumps make 0509 most consistent with a $1M_{\odot}$ WD explosion, although a near- M_{ch} WD explosion with unburnt He in the ejecta cannot be ruled out. They also favor a large explosion energy ($\approx 1.5 \times 10^{51}$ erg) and note that this energy is available via detonation of a WD with a $0.85M_{\odot}$ carbon-oxygen (CO) core and a $0.15M_{\odot}$ helium (He) shell. Recent optical tomography of 0509 from the deep MUSE (Multi Unit Spectroscopic Explorer) data revealed a double shell [Ca xv] and a single shell [S xii] morphology in the ejecta (Das et al. 2025). Their study suggested that this signature can be expected from the double detonation of a CO WD with $\sim 1M_{\odot}$ core and a helium shell of $\sim 0.03M_{\odot}$.

Thus far, the general consensus has been that sub- M_{ch} models are rather poor matches to the 1991T-like spectral subtype. The main reason is that the typical absolute magnitudes ($M_B < -19.5$ mag) and decline rates ($\Delta m_{15}(B) = 0.95 \pm 0.05$) for 1991T-like SNe (Phillips et al. 2022, 2024, and references therein) require large WD masses and ^{56}Ni masses, which are not typical for sub- M_{ch} models. Though it has been suggested that double detonation explosions could reproduce the peculiar Fe absorption features in the pre-maximum phase optical spectra of 1991T-like SNe (Filippenko et al. 1992), recent studies find discrepancies between spectral properties of sub- M_{ch} models and 1991T-like SNe. For instance, the peak B-band magnitude (M_B) and the Si II velocity of 1991T-like SNe suggest a near- M_{ch} origin rather than a sub- M_{ch} one (Polin et al. 2019, 2021). Moreover, Polin et al. (2021) find that the [Ca II]/[Fe III] ratio in the optical nebular spectra of luminous (including 1991T-like) SNe is overproduced by double detonation models.

Unlike early time supernovae, the SNR 0509 is in a late enough stage of evolution for its ejecta structure to be spatially resolved (~ 400 yrs; Rest et al. 2005), yet not evolved enough for its ejecta to have mixed substantially with gas from the interstellar medium (ISM). It is thus an excellent testbed for probing whether 1991T-like SNe can result from double detonations. In this work, we analyze optical coronal line maps of 0509 (Fig. 1) to study its small-scale substructures, following Mandal et al. (2024). These substructures result from turbulent activity as the SNR expands against the ambient medium (Chevalier & Klein 1978; Chevalier et al. 1992) and bear signatures of the outermost layers of the stellar ejecta (Polin et al. 2022; Mandal et al. 2023). Mandal et al. (2025) show that the typical size of IGE-dominated substructures tend to be bigger than IME-dominated substructures in Type Ia SNRs with sub- M_{ch} progenitors, whereas both classes of substructures are comparable in size for SNRs formed from near- M_{ch} WDs.

To investigate the nature of the substructures in 0509 further, we develop three-dimensional SNR models formed from double detonation explosions and analyze small-scale structures in these models using power spectral analysis. Moreover, our study allows us to independently test the conjecture regarding the progenitor WD mass by Seitenzahl et al. (2019) and the explosion mechanism by Das et al. (2025) from a different approach, providing further constraints on the core and shell masses of the progenitor WD.

This work is organized as follows: The observational data used in this work are described in Section 2. Details of the SNR models and the techniques used to analyze the models and the data are discussed in Section 3. The results are presented in Section 4, and a summary of the results is presented in Section 5.

2. OBSERVATIONAL DATA

A deep observational campaign targeting the supernova remnant SNR 0509 was carried out using the Multi Unit Spectroscopic Explorer (MUSE; Bacon et al. 2010), an optical integral field spectrograph mounted on Unit Telescope 4 (UT4) of the European Southern Observatory’s (ESO) Very Large Telescope at Cerro Paranal. This effort was part of ESO program 0104.D-0104(A), led by P.I. Seitenzahl. Observations were conducted in service mode using the Wide Field Mode with Adaptive Optics (WFM-AO) configuration, spread over 25 nights across a 24-month period (see Methods in Das et al. 2025). A total of 40 exposures were obtained: 39 of these were approximately 2700 seconds in duration, while one shorter observation lasting 93.92 seconds was discarded due to poor data quality. The resulting dataset comprises a total exposure time of roughly 105,300 seconds (equivalent to 29 hours and 15 minutes). Each MUSE data cube covers the optical wavelength range from 4690 Å to 9340 Å at a spectral resolution of $R \sim 3000$. To minimize contamination from the laser guide stars of the 4LGSF system, a notch filter is employed in WFM-AO mode to block the spectral region from 5804 Å to 5965 Å (Vogt et al. 2018; Vogt et al. 2017). However, this filter does not completely eliminate the effects of Raman-scattered photons originating from the laser light. These residual artifacts are subsequently identified and removed during data processing using the MUSE data reduction pipeline (Weilbacher et al. 2020).

Data reduction was performed using ESOREflex (Freudling et al. 2013) version 2.11.5 and the MUSE data reduction pipeline version 2.8.9 (Weilbacher et al. 2020), both run with default settings. The process included the removal of known sky lines and was carried out on Tycho, a high-memory Linux workstation at the

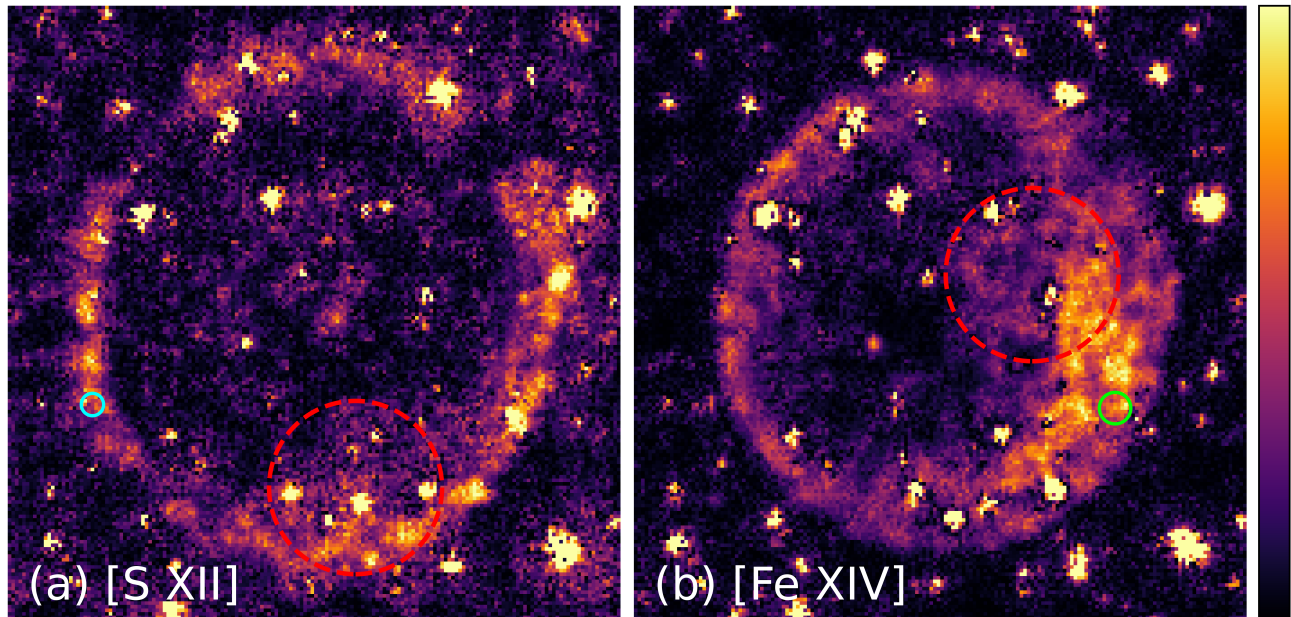


Figure 1. [S XII] (*left*) and [Fe XIV] (*right*) emissivity distributions in SNR 0509-67.5. Circles corresponding to spherical harmonics $l \approx 30$ (solid cyan) and $l \approx 20$ (solid green) are overlaid on the S and Fe images, respectively. A circle of radius corresponding to $l = 4$ (dotted red) is also marked on both images. These harmonics correspond to bends in the power spectra of 0509 (shown in Fig. 3) and likely to the small scale clumps in these images.

University of New South Wales in Canberra, specifically configured for handling MUSE data. Since no dedicated sky observations were available, background subtraction was performed using the pipeline’s alternative method: computing a sky model from a specified portion of the field of view, controlled by the parameter `SkyFr.2`. All individual data cubes were stored in a single directory, used as the pipeline’s input (with no additional calibration files). The final mosaic was produced by re-running the pipeline with the 39 reduced MUSE pixel tables as input, combining them into a single data cube. This mosaic covers a $1' \times 1'$ field of view, with a spatial sampling of $0.2'' \times 0.2''$ per spaxel, and was used for all subsequent analysis. Since our primary areas of interest are the broad coronal emission lines from the reverse shocked ejecta, the conventional background subtraction is not sufficient as these signals have 170 times lower spectral flux compared to $H\alpha$. The final mosaic data cube was processed with an additional background subtraction and galactic de-reddening (Das et al. 2025; Ghavamian et al. 2017, see details). The data cube was then smoothed by using a Gaussian smoothing with `kernel=2` in `QFitsView` for better visualization of fainter structures. [Fe XIV] $\lambda 5303 \text{ \AA}$ and [S XII] $\lambda 7611 \text{ \AA}$ emission are visualized by integrating the spectra over specific wavelength intervals (λ_1 and λ_2) corresponding to the emission features of each forbidden line. To remove the underlying stellar continuum, adjacent spectral re-

gions on either side of the emission line ($\Delta\lambda_{*1}$ and $\Delta\lambda_{*2}$) are also integrated and subtracted from the signal. The chosen wavelength ranges for both the emission features and the surrounding continua are listed in Table 1.

3. NUMERICAL METHOD

3.1. Initial conditions

We use angle-averaged (1D) versions of DD models described in Gronow et al. (2021), hosted on the HESMA project (Kromer et al. 2017) website². These models span a range of CO core masses and He shell masses. The ejecta density profile and abundance profiles for S and Fe from these models are mapped onto a 3D domain and allowed to expand to the SNR phase (described in the next Section). The ejecta are assumed to be cold ($P = 10^{-6}\rho$) and expanding homologously ($v = r/t$). The ambient medium is set to have uniform density. The details of these models are listed in Table 2.

3.2. Remnant evolution and analysis

The 1D models are mapped onto a 3D Cartesian grid in `Sprout`, a second-order ideal hydrodynamics code (Mandal & Duffell 2023) designed to studying expanding outflows. `Sprout` utilizes the moving mesh paradigm (Springel 2010; Duffell & MacFadyen 2011) to expand

² <https://hesma.h-its.org>

Coronal Emission Lines	$\lambda_1(\text{\AA})$	$\lambda_2(\text{\AA})$	$\Delta\lambda_{*1}(\text{\AA})$	$\Delta\lambda_{*2}(\text{\AA})$	Peak Surface Brightness ($\text{ergs}^{-1}\text{cm}^{-2}\text{arcsec}^{-2}$)
[Fe XIV]	5218	5364	5150 - 5190	5485 - 5528	6.77×10^{-17}
[S XII]	7602	7705	7393 - 7484	7779 - 7809	2.67×10^{-17}

Table 1. Spectral windows used to remove stellar continuum and isolate emission from ionized species.

Table 2. Summary of the DD SN models used in this work.

Name	Core mass (in M_\odot)	Shell mass (in M_\odot)
M0803	0.8	0.03
M0805	0.8	0.05
M0903	0.9	0.03
M0905	0.9	0.05
M0910	0.9	0.10
M1003	1.0	0.03
M1005	1.0	0.05
M1010	1.0	0.10

its computational domain with time, following the evolution of the SNR. The expanding grid provides a high dynamic range in resolution. This is necessary to model the SNR's expansion, which starts at 100s and continues till 600yrs. The end time is chosen keeping in mind the age estimate of SNR 0509-67.5, which is roughly in the range 300 – 500 yrs (Rest et al. 2005; Hovey et al. 2015).

It is convenient to describe the time evolution of the SNR models in terms of a dimensionless quantity t_D , called the dynamical age of the remnant. This is essentially the age of the remnant (t) divided by the characteristic time or Sedov time (T_c), which is the time taken by the forward shock to sweep up mass comparable to the ejecta mass itself. The characteristic time is a function of the ejecta mass M , explosion energy E , and ambient medium (AM) density (Truelove & McKee 1999; Warren & Blondin 2013; Mandal et al. 2024). Using this, we can define the dynamical age t_D as follows:

$$t_D \equiv \left(\frac{t}{628\text{yrs}} \right) \left(\frac{M}{M_{ch}} \right)^{5/6} E_{51}^{-1/2} n_0^{-1/3}, \quad (1)$$

where $M_{ch} = 1.4M_\odot$ is the Chandrasekhar mass, $E_{51} = E/(10^{51}\text{ergs})$, and n_0 is the AM density in units of amu cm^{-3} . Note that this definition is not unique. For example, Warren & Blondin (2013) choose a different characteristic age T' , which is related to our choice as $T' = 0.43T_c$.

The power spectra of these 3D models are extracted at several instant of times, using the method outlined in

Polin et al. (2022) and Mandal et al. (2023). Spherical surface distributions of the radially integrated density distributions of Si (and Fe) are calculated for each model snapshot as follows:

$$\langle \rho_{Si} \rangle (\theta, \phi) = \frac{\int X_{Si} P \rho dr}{\int X_{Si} P dr}, \quad (2)$$

where X_{Si} is the passive scalar representing the mass fraction of Si. Pressure weighting ensures that only the shocked, turbulent region is used for this calculation. These spherical surface distributions are expanded in terms of spherical harmonics using the SHTOOLS package (Wieczorek & Meschede 2018). This allows us to derive a power spectrum C_l in terms of the spherical harmonic l (see Eqns. 11 and 12 of Mandal et al. 2024).

3.3. Image analysis

The substructure size distributions in the images of 0509 are measured using the Δ -variance algorithm (Arévalo et al. 2012), as adapted by Mandal et al. (2024). This technique computes a low resolution power spectrum of a two-dimensional image, as is the case here. It is to be noted that this power spectrum is not necessarily equivalent to those of 3D models we describe in Section 3.2. However, Mandal et al. (2024) showed that power spectra of their 3D SNR models are equivalent to the Δ -variance-based power spectra of synthetic images corresponding to the same models, for spherical harmonics $l \gtrsim 10$. Therefore, in this work we treat the power spectra of 0509 images as those that one would obtain upon analysis of the full 3D distribution of the ejecta in 0509. In other words, the Δ -variance-based power spectra of 0509 images are directly compared to those of our 3D models. Since Δ -variance computes power as a function of lengthscale σ (in pixel units), it has to be converted to the angular harmonic l as shown by Mandal et al. (2024):

$$l \approx 1.6R_{SNR}/\sigma, \quad (3)$$

where R_{SNR} is the radius of the image of the SNR, also in pixel units. We apply masks on the foreground stars to ensure they are not contaminating our analysis.

4. RESULTS

4.1. Power spectral analysis of numerical models

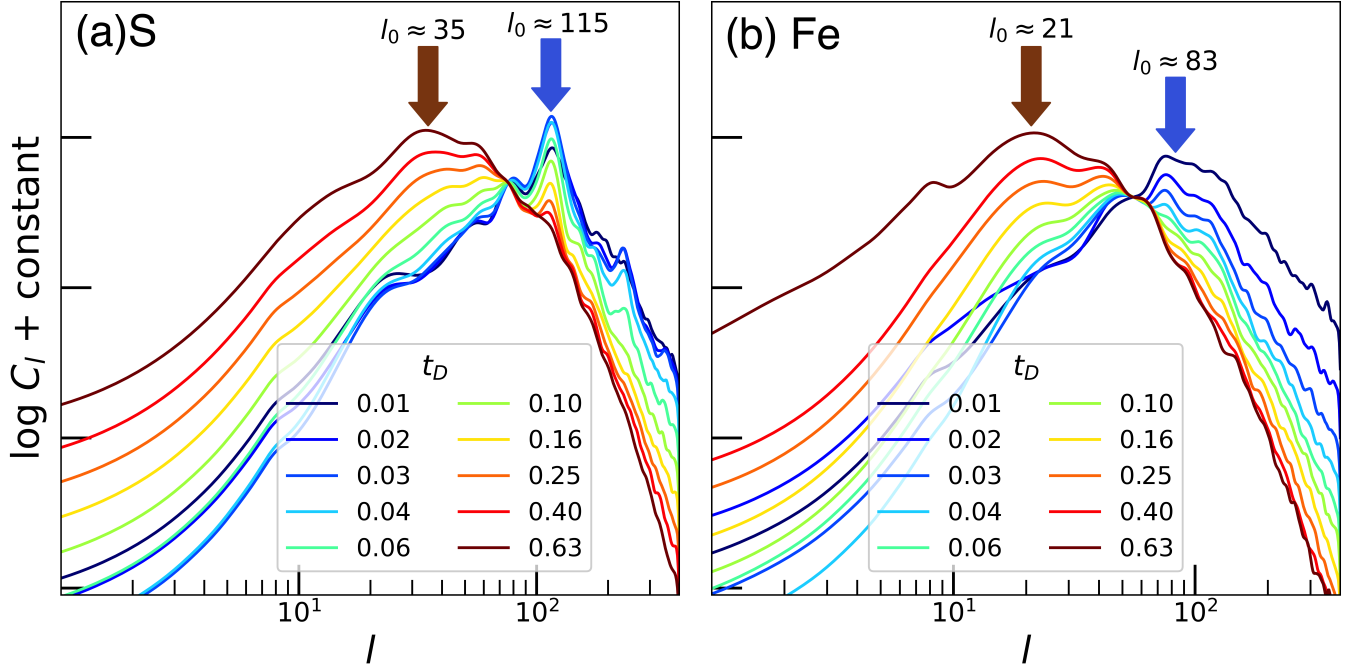


Figure 2. Power spectrum of S (*left*) and Fe (*right*) distributions in the ejecta of the M1003 model, evaluated at 10 logarithmically spaced time instants in the range $t_D = 0.01 - 0.63$. All power spectra have a broken power-law shape. The wavenumber where the power spectrum changes slope or peaks (l_0) corresponds to the lengthscale where most of the power in the turbulent substructures reside. With time, l_0 shifts to smaller values, indicating growth of RTI structures. For DD SNRs, l_0 of S distribution (l_0^S henceforth) consistently remains larger than the l_0 for Fe distribution (l_0^{Fe} henceforth). For example, at $t_D = 0.01$, $l_0^S \approx 115$, while $l_0^{\text{Fe}} \approx 83$.

Power spectra of hydrodynamic SNR models without large scale asymmetries are expected to have a broken power-law form (Warren & Blondin 2013; Polin et al. 2022; Mandal et al. 2023)³:

$$C_l \propto \frac{1}{(l/l_0)^{-n_1} + (l/l_0)^{n_2}}, \quad (4)$$

where l_0 is the wavenumber at which the power spectrum peaks. The power spectra can be approximated at $l \lesssim l_0$ as $C_l \propto l^{n_1}$, and at $l \gtrsim l_0$ as $C_l \propto l^{-n_2}$, with n_1 and n_2 being positive. The peak wavenumber l_0 corresponds to the typical size of the most powerful turbulent eddies formed in the ejecta-AM interaction of the SNR.

Our double detonation SNR models show a similar behavior. In Fig. 2, we plot the power spectra of S (left panel) and Fe (right panel) distributions in the M1003 model at various instants of time. The power spectra of S and Fe represent those of IMEs and IGEs, respectively. Power spectra at early times are plotted in blue, and the colors transition to red at late times. For both panels, l_0 decreases with time, that is, the peak shifts to the left. This behavior can be understood by noting that l_0 is

roughly proportional to the effective power-law slope of the ejecta encountered by the reverse shock (Polin et al. 2022; Mandal et al. 2024). This result suggests that the typical size of turbulent eddies in SNRs is of the order of the density scale height at the reverse shock. Since the ejecta density falls off steeply at large radii but is relatively shallow in the inner regions (for an example, see Figure 2 of Collins et al. 2025), the reverse shock encounters shallower density profiles as it moves deeper into the ejecta. Thus the value of the ejecta power-law slope encountered by the reverse shock increases with age.

The value of l_0 thus provides us an estimate of the dynamical age of an SNR (Mandal et al. 2024). Moreover, at every instant of time, the value of l_0 for the power spectrum of IMEs (l_0^S henceforth) is seen to be greater than the value of l_0 for the power spectrum of IGEs (l_0^{Fe} henceforth). This is an exclusive signature of SNRs with sub- M_{ch} WD progenitors (Mandal et al. 2025). This property stems from the fact that near- M_{ch} Type-Ia SN progenitors generate a lot of buoyant ashes from their initial deflagration phase that cause significant mixing in the ejecta. The sub- M_{ch} WD progenitors are expected to experience detonations (or supersonic nuclear flame fronts) only, that do not cause this amount of mixing and therefore retain stratification in

³ There can be deviations from this shape if large scale asymmetries are present, see Ferrand et al. (2021) for examples.

their ejecta. This causes the IMEs and IGEs to participate at different times in the ejecta-AM interaction and therefore develop substructures with different typical sizes (see Section 4.4 of Mandal et al. 2025). This holds true for all our DD SNR models, as will be seen in Section 4.3. This

4.2. Substructure analysis of SNR 0509-67.5

Fig. 3 shows the power spectra obtained from the [Fe XIV] and [S XII] images of 0509. Both of them have strong bumps or peaks at $l = 4$. The presence of large power at such a small wavenumber evidently comes from the large scale asymmetry visible in 0509. In addition, the Fe power spectrum shows a break or change in slope at $l \sim 20$, while the S power spectrum shows a break at $l \sim 30$.

Following Mandal et al. (2024, 2025), we interpret these breaks as the RTI peak l_0 for the Fe and S distributions, respectively. Either power spectrum for 0509 may thus be viewed as a broken power-law corresponding to RTI activity, plus a large bump at $l \approx 4$ accounting for large-scale asymmetries inherent to the ejecta. As a sanity check for this interpretation, we overlay the S and Fe distribution images in Fig. 1 with circles of radii corresponding to $l = 4, 20$ and 30 , calculated using Eqn. 3. Visual inspection shows that the bump at $l = 4$ likely corresponds to prominent large scale structures (likely locations marked with red circles in Fig. 1) in 0509. Moreover, the lengthscales corresponding to $l = 20$ and $l = 30$ appear to be similar to the small-scale substructures in 0509 (see, e.g., the alternately bright and dark circular patches in northwestern part of the [Fe XIV] emission in Fig. 1b).

Based on the arguments above, we adopt the view that the breaks in the power spectra of 0509 correspond to the RTI peaks in the power spectra of our SNR models. To identify these break wavenumbers accurately, we fit the power spectra of S and Fe distributions in 0509 to the sum of two broken power laws (both components are as in Eqn. 4), one corresponding to RTI activity and the other to large scale intrinsic asymmetry in the ejecta. For the power spectrum of S distribution, the fit provides $l_0 (= l_0^S) = 31 \pm 2$ and $n_2 = 2.16 \pm 0.05$. For the power spectrum of Fe distribution, the fit provides $l_0 (= l_0^{\text{Fe}}) = 22 \pm 1$ and $n_2 = 2.50 \pm 0.04$. Considering the radius of 0509 as observed in the sky is $\approx 15''$ (Arunachalam et al. 2022), we find the typical size of S and Fe dominated substructures seen in Fig. 1 to be $\approx 0.8''$ and $\approx 1.1''$ respectively (using Eqn. 3 and the values of l_0^S and l_0^{Fe}).

We find $l_0^S/l_0^{\text{Fe}} = 1.42 \pm 0.20$. As mentioned in Section 1, Mandal et al. (2025) show that such values of the power spectra peak wavenumber ratio (of IMEs to

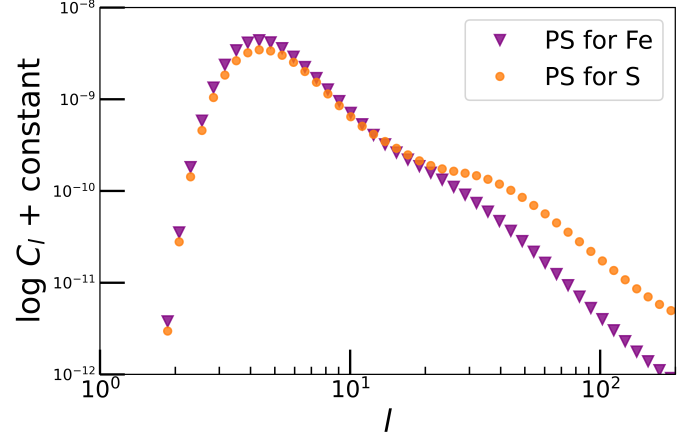


Figure 3. Power spectra of S and Fe distributions in SNR 0509-67.5. Both power spectra show a strong bump at $l \approx 4$, which is anticipated given the presence of the prominent large scale asymmetric features in 0509. Both curves also show a bend or change in slope at $l \approx 30$ and $l \approx 20$, which likely corresponds to small scale clumps seen in 0509 (see Fig. 1).

IGEs) favor a sub- M_{ch} WD progenitor, while an SNR with a near- M_{ch} WD progenitor would have the ratio l_0^S/l_0^{Fe} almost exactly equal to unity. The steep nature of the power spectra of S and Fe for large l ($|n_2| > 5/3$) also matches characteristics of the power spectra of our models, confirming the absence of a turbulent cascade in 0509.

4.3. Trends in l_0^S and l_0^{Fe} of double detonation SNRs: implications for SNR 0509-67.5

In Fig 4, we plot the time evolution of l_0^S (top panel) and l_0^{Fe} (bottom panel) for all of our models. The general trend of l_0 decreasing with time is observed. In addition, all l_0 values asymptote to a minimum at late times, as also noted by Mandal et al. (2024). We also overlay the panels with the most likely range of l_0^S and l_0^{Fe} for 0509 (as obtained in Section 4.2), along with the possible range of dynamical age (t_D) of 0509, which has to be calculated using estimates of its age and Sedov time (T_c). The age of 0509 is estimated to be 400 ± 120 years from light echo modeling (Rest et al. 2005). The Sedov time is calculated assuming an ejecta mass of $1 M_{\odot}$, an explosion energy of 1.5×10^{51} ergs and ambient number density of 0.4 cm^{-3} , as suggested by Seitenzahl et al. (2019) on the basis of shock dynamics and emission measures observed in 0509. Using these values in Eqn. 1, we obtain a range of $t_D = 0.43 - 0.80$.

The top panel of Fig. 4 shows that the asymptotic value of l_0^S at late times is dependent upon the core mass. Models with lower core mass (M0803 and 0805; dashed lines) exhibit a lower asymptotic value of l_0^S in comparison to higher core mass models. In other words,

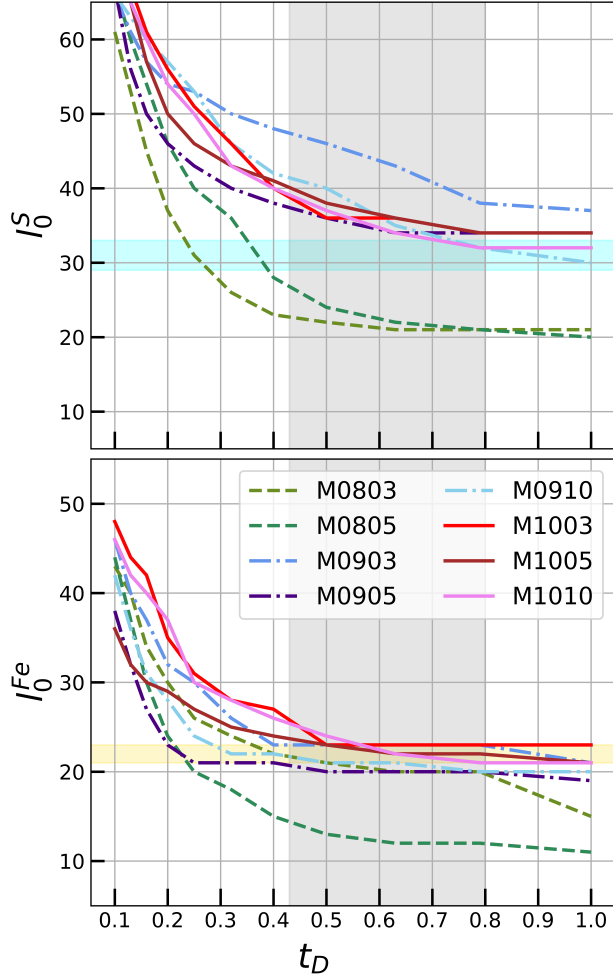


Figure 4. Evolution of l_0^S (top) and l_0^{Fe} (bottom) with time for all DD SNR models. Results for models with core masses of $0.8M_\odot$, $0.9M_\odot$ and $1.0M_\odot$ have been plotted with dashed, dash-dotted, and solid lines respectively for ease of viewing. These plots have been overlaid with the range of l_0^S ($= 31 \pm 2$) and l_0^{Fe} ($= 22 \pm 1$) obtained from our fit for the power spectra of 0509, along with the likely range of dynamical age (t_D) of 0509.

lower core mass models tend to form larger IME clumps in comparison to their higher core mass counterparts. This trend is not monotonic, since the asymptotic value of l_0^S for the model M0903 is found to be greater than the same for the M10xx models, but a stark difference is found between the models with core mass above and below $0.8M_\odot$. In contrast, l_0^S isn't found to be sensitive to the mass of the He shell.

The bottom panel of Fig. 4 shows that the asymptotic value of l_0^{Fe} is lower than that of l_0^S for each model, as expected. At first glance, it appears that no clear trend exists for the asymptotic values of l_0^{Fe} amongst the models. However, focusing on a particular value of core mass, one finds that the models with lower shell masses have

a lower asymptotic value of l_0^{Fe} (compare the l_0^{Fe} curves for M0803 and M0805, for example). Regardless, there is sufficient degeneracy in l_0^{Fe} due to the varying core masses of our models that it would be difficult to constrain the shell mass unless the core mass were known accurately.

Comparing the values of l_0^S in our models to those found for 0509, we find that models with mass $\leq 0.8M_\odot$ are not consistent with 0509. The only models favored by the l_0^S measurements are M0910 and M1010. The value of l_0^S measured for 0509 also restricts us to $t_D \gtrsim 0.7$, as can be seen from the top panel of Fig. 4. Looking at the range $0.7 < t_D < 0.8$ in the bottom panel of Fig. 4, we see that the measured value of l_0^{Fe} in 0509 favors the M0903, M1003, M1005, and M1010 models. We therefore conclude that M1010 is the only model in our suite that satisfactorily reproduces observed values of both l_0^S and l_0^{Fe} in 0509 at the same time. Note that M0910 does reproduce values of l_0^S and l_0^{Fe} observed for 0509, but not at the same value of t_D . However, considering uncertainties in our numerical and observational analysis, we err on the side of caution and suggest that 0509 has a WD progenitor with a core mass of $0.9 - 1.0M_\odot$ and a shell mass of $0.05M_\odot < M \lesssim 0.1M_\odot$. We also note that our SNR models do not examine the range between $0.05M_\odot < M < 1.0M_\odot$ for the He shell mass due to limited availability of DD models, and hence cannot conclusively rule out models in this range.

We note that this constraint holds even if one estimates t_D for 0509 assuming a near- M_{ch} WD progenitor, unlike our calculation. For instance, Arumachalam et al. (2022) favor a near- M_{ch} origin for 0509, on the basis of forward shock kinematics measured using Hubble H α observations. Assuming $E_{51} = 1.4$, they obtain $M = 2.02 \pm 0.85M_\odot$, $\log \rho_0 = -24.23 \pm 0.09$, and an age of $t = 329.7 \pm 17.3$ years for 0509. Alternatively, holding M fixed to $1.4M_\odot$, they estimate probable ranges $E_{51} = 1.30 \pm 0.41$, $\log \rho_0 = -24.20 \pm 0.20$, and an age of $t = 317.19 \pm 12.95$ years. Using these values, we obtain a range of $t_D = 0.65 - 0.95$. As Fig. 4 shows, this range of t_D still favors the M1010 model when the values of both l_0^S and l_0^{Fe} are considered.

The M1010 model has an ejecta mass of $1.1M_\odot$ and kinetic energy $\approx 1.5 \times 10^{51}$ ergs. Also taking the age of 0509 to be 400 ± 120 years (Rest et al. 2005), we can compute a range of dynamical age for 0509 using Eqn. 1:

$$t_D = \left(\frac{400 \pm 120 \text{ yrs}}{628 \text{ yrs}} \right) \left(\frac{1.1M_\odot}{1.4M_\odot} \right)^{5/6} 1.5^{-1/2} n_0^{-1/3} \quad (5)$$

$$= 0.43 \pm 0.13 n_0^{-1/3}.$$

Comparing this to the range $0.7 < t_D < 0.8$ predicted by our analysis, we obtain a range of AM densities $0.05 < n_0 < 0.5$ (in units of amu cm^{-3}) for 0509. This is a rather broad range, but is consistent with all previous estimates for the AM density around 0509 (Seitenzahl et al. 2019; Arunachalam et al. 2022).

5. DISCUSSION

In this work, we have developed three dimensional models of Type Ia SNRs exploding via the double detonation (DD) mechanism, using pre-computed DD SN models described in Gronow et al. (2021). We analyze the typical size of substructures formed in these SNR models as a result of turbulent activity in the expanding SNR. We also compute the typical size of silicon and iron dominated substructures in the 0509, using high resolution MUSE observations. We find that spherical wavenumbers corresponding to the typical size of silicon-dominated and iron-dominated substructures in SNR 0509-67.5 are given by $l_0^S = 31 \pm 2$ and $l_0^{\text{Fe}} = 22 \pm 1$, respectively. These wavenumbers represent lengthscales that are $\approx 5\%$ and $\approx 7\%$ of the radius of the remnant, respectively (see Eqn. 3). This disparity between IME and IGE dominated substructures is a key signature of a sub- M_{ch} WD progenitor in Type Ia SNRs, as has been shown before (Mandal et al. 2025). Our study thus provides novel and independent evidence to the suggestion that SNR 0509 originated from the double detonation of a sub- M_{ch} CO WD (Das et al. 2025). Furthermore, comparing to our suite of SNR models spanning a range of carbon-oxygen core mass and helium shell mass, we find 0509 to be the most consistent with the explosion of a WD with a core and shell mass of $1M_{\odot}$ and $0.05M_{\odot} < M \lesssim 0.1M_{\odot}$, respectively. The total ejecta mass and energy ($\approx 1.5 \times 10^{51}$ ergs) of this model is found to be in good agreement with the prediction of Seitenzahl et al. (2019).

As mentioned in Section 1, 0509 is also associated with a 1991T-like event based on light echo reconstruction of spectra (Rest et al. 2008). These SNe are bright and fade slowly. The M1010 model also exhibits high maximum absolute bolometric magnitudes ($M_{\text{bol,max}} \sim -19.5$) and slow decline rates ($\Delta m_{15,\text{bol}} \sim 0.95$), at least in some viewing directions (see Fig. 6 of Gronow et al. 2021). It's important to note that lightcurves of the M1010 model cannot adequately match that of SN 1991T (Collins et al. 2022) despite this apparent similarity. But, recent non-LTE radiative transfer calcu-

lations suggest that the double detonation model may be able to yield lightcurves and spectra that agree with observations of both normal and overluminous Type-Ia SNe (Shen et al. 2021; Collins et al. 2025). In fact, a recent study by O'Brien et al. (2024) suggests that 1991T-like SNe may be an extension of normal Type Ia SNe, with the only observational difference between these subclasses lying in the elemental abundances and ionization fractions. Recent observations of SN 2022joj (Padilla Gonzalez et al. 2024) and 2020eyj (Kool et al. 2023) have also pointed towards the possible origin of 1991T-likes from a double detonation event. Another possible explanation of the apparent disagreement between double detonation models and 1991T-like SNe is the presence of dense circumstellar medium (CSM) in the vicinity of SN 1991T, which would aid in conversion of kinetic energy of the ejecta to radiated energy. This has been proposed by Leloudas et al. (2015), who find an association between 1991T-like SNe and SNe Type Ia-CSM (Type Ia SNe interacting with dense CSM). They suggest that 1991T-like SNe are likely born in single degenerate systems generating dense CSM due to mass loss from the main sequence companion.

As of now, no explosion models can completely explain the observed features of 1991T-like SNe due to inherent multidimensional nature of the explosion (Pakmor et al. 2024). Given the growing line of evidence that SNR 0509-67.5 originated from a double detonation (Das et al. 2025, and this work), we encourage future works on the double detonation model to investigate the effects of multidimensionality and non-LTE on their lightcurves and spectra, as well as study the connection between 1991T-like events and double detonation SN models with dense CSM.

ACKNOWLEDGMENTS

This work made use of the Heidelberg Supernova Model Archive (HESMA), <https://hesma.h-its.org>. Numerical calculations were performed on the Rivanna computing cluster at University of Virginia. P.G. acknowledges support from the Maryland Space Grant Consortium and NASA.

Software: Sprout (Mandal & Duffell 2023), VisIt (Childs et al. 2012), SHTOOLS (Wieczorek & Meschede 2018), NumPy (Harris et al. 2020), Matplotlib (Hunter 2007), Astropy.

REFERENCES

- Aleo, P. D., Malanchev, K., Sharief, S., et al. 2023, ApJS, 266, 9
- Arévalo, P., Churazov, E., Zhuravleva, I., Hernández-Monteagudo, C., & Revnivtsev, M. 2012, MNRAS, 426, 1793

- Arnett, W. D. 1969, *Ap&SS*, 5, 180
- Arnett, W. D., Truran, J. W., & Woosley, S. E. 1971, *ApJ*, 165, 87
- Arunachalam, P., Hughes, J. P., Hovey, L., & Eriksen, K. 2022, *ApJ*, 938, 121
- Bacon, R., Accardo, M., Adjali, L., et al. 2010, in *Ground-based and Airborne Instrumentation for Astronomy III*, Vol. 7735, SPIE, 131–139
- Badenes, C., Borkowski, K. J., Hughes, J. P., Hwang, U., & Bravo, E. 2006, *ApJ*, 645, 1373
- Badenes, C., Hughes, J. P., Cassam-Chenaï, G., & Bravo, E. 2008, *ApJ*, 680, 1149
- Bora, Z., Könyves-Tóth, R., Vinkó, J., et al. 2024, *PASP*, 136, 094201
- Bozzetto, L. M., Filipović, M. D., Urošević, D., Kothes, R., & Crawford, E. J. 2014, *MNRAS*, 440, 3220
- Chandrasekhar, S. 1931, *ApJ*, 74, 81
- Chevalier, R. A., Blondin, J. M., & Emmering, R. T. 1992, *ApJ*, 392, 118
- Chevalier, R. A., & Klein, R. I. 1978, *ApJ*, 219, 994
- Childs, H., Brugger, E., Whitlock, B., et al. 2012, in *High Performance Visualization—Enabling Extreme-Scale Scientific Insight* (Chapman and Hall/CRC), 357–372
- Collins, C. E., Gronow, S., Sim, S. A., & Röpke, F. K. 2022, *MNRAS*, 517, 5289
- Collins, C. E., Shingles, L. J., Sim, S. A., et al. 2025, *MNRAS*, 538, 1289
- Das, P., Seitzzahl, I. R., Ruiter, A. J., et al. 2025, *Nature Astronomy*, doi:10.1038/s41550-025-02589-5
- DES Collaboration, Abbott, T. M. C., Acevedo, M., et al. 2024, *ApJL*, 973, L14
- Duffell, P. C., & MacFadyen, A. I. 2011, *ApJS*, 197, 15
- Ferrand, G., Tanikawa, A., Warren, D. C., et al. 2022, *ApJ*, 930, 92
- Ferrand, G., Warren, D. C., Ono, M., et al. 2021, *ApJ*, 906, 93
- Filippenko, A. V., Richmond, M. W., Matheson, T., et al. 1992, *ApJL*, 384, L15
- Fink, M., Hillebrandt, W., & Röpke, F. K. 2007, *A&A*, 476, 1133
- Fink, M., Röpke, F. K., Hillebrandt, W., et al. 2010, *A&A*, 514, A53
- Flörs, A., Spyromilio, J., Taubenberger, S., et al. 2020, *MNRAS*, 491, 2902
- Freudling, W., Romaniello, M., Bramich, D., et al. 2013, *A&A*, 559, A96
- Gal-Yam, A. 2017, in *Handbook of Supernovae*, ed. A. W. Alsabti & P. Murdin, 195
- Ghavamian, P., Blair, W. P., Sankrit, R., Raymond, J. C., & Hughes, J. P. 2007, *ApJ*, 664, 304
- Ghavamian, P., Seitzzahl, I. R., Vogt, F. P. A., et al. 2017, *ApJ*, 847, 122
- Gronow, S., Collins, C. E., Sim, S. A., & Röpke, F. K. 2021, *A&A*, 649, A155
- Hansen, C. J., & Wheeler, J. C. 1969, *Ap&SS*, 3, 464
- Harris, C. R., Millman, K. J., van der Walt, S. J., et al. 2020, *Nature*, 585, 357
- Helder, E. A., Kosenko, D., & Vink, J. 2010, *ApJL*, 719, L140
- Hillebrandt, W., Kromer, M., Röpke, F. K., & Ruiter, A. J. 2013, *Frontiers of Physics*, 8, 116
- Hovey, L., Hughes, J. P., & Eriksen, K. 2015, *ApJ*, 809, 119
- Hunter, J. D. 2007, *Computing in Science & Engineering*, 9, 90
- Ivanova, L. N., Imshennik, V. S., & Chechetkin, V. M. 1974, *Ap&SS*, 31, 497
- Ivezić, Ž., Kahn, S. M., Tyson, J. A., et al. 2019, *ApJ*, 873, 111
- Iwamoto, K., Brachwitz, F., Nomoto, K., et al. 1999, *ApJS*, 125, 439
- Kepler, S. O., Kleinman, S. J., Nitta, A., et al. 2007, *MNRAS*, 375, 1315
- Khokhlov, A. M. 1991a, *A&A*, 245, 114
- . 1991b, *A&A*, 245, L25
- Kirshner, R. P. 2010, in *Dark Energy: Observational and Theoretical Approaches*, ed. P. Ruiz-Lapuente, 151
- Kochanek, C. S., Shappee, B. J., Stanek, K. Z., et al. 2017, *PASP*, 129, 104502
- Kool, E. C., Johansson, J., Sollerman, J., et al. 2023, *Nature*, 617, 477
- Kosenko, D., Vink, J., Blinnikov, S., & Rasmussen, A. 2008, *A&A*, 490, 223
- Kromer, M., Ohlmann, S., & Röpke, F. K. 2017, *Mem. Soc. Astron. Italiana*, 88, 312
- Lach, F., Röpke, F. K., Seitzzahl, I. R., et al. 2020, *A&A*, 644, A118
- Law, N. M., Kulkarni, S. R., Dekany, R. G., et al. 2009, *PASP*, 121, 1395
- Leloudas, G., Hsiao, E. Y., Johansson, J., et al. 2015, *A&A*, 574, A61
- Livne, E. 1990, *ApJL*, 354, L53
- Mandal, S., & Duffell, P. C. 2023, *The Astrophysical Journal Supplement Series*, 269, 30
- Mandal, S., Duffell, P. C., Polin, A., & Milisavljevic, D. 2023, *ApJ*, 956, 130
- . 2024, *ApJ*, 972, 87
- Mandal, S., Torres-Albà, N., Badenes, C., & Mohamed, S. 2025, *arXiv e-prints*, arXiv:2508.10752
- Maoz, D., & Graur, O. 2017, *ApJ*, 848, 25

- Niemeyer, J. C., Hillebrandt, W., & Woosley, S. E. 1996, *ApJ*, 471, 903
- Niemeyer, J. C., & Woosley, S. E. 1997, *ApJ*, 475, 740
- Nomoto, K., Saio, H., Kato, M., & Hachisu, I. 2007, *ApJ*, 663, 1269
- Nomoto, K., Thielemann, F. K., & Yokoi, K. 1984, *ApJ*, 286, 644
- O’Brien, J. T., Kerzendorf, W. E., Fullard, A., et al. 2024, *ApJ*, 964, 137
- Padilla Gonzalez, E., Howell, D. A., Terreran, G., et al. 2024, *ApJ*, 964, 196
- Pakmor, R., Kromer, M., Röpke, F. K., et al. 2010, *Nature*, 463, 61
- Pakmor, R., Kromer, M., Taubenberger, S., et al. 2012, *ApJL*, 747, L10
- Pakmor, R., Seitenzahl, I. R., Ruiter, A. J., et al. 2024, *A&A*, 686, A227
- Perley, D. A., Fremling, C., Sollerman, J., et al. 2020, *ApJ*, 904, 35
- Phillips, M. M. 1993, *ApJL*, 413, L105
- Phillips, M. M., & Burns, C. R. 2017, in *Handbook of Supernovae*, ed. A. W. Alsabti & P. Murdin, 2543
- Phillips, M. M., Ashall, C., Burns, C. R., et al. 2022, *ApJ*, 938, 47
- Phillips, M. M., Ashall, C., Brown, P. J., et al. 2024, *ApJS*, 273, 16
- Polin, A., Duffell, P., & Milisavljevic, D. 2022, *The Astrophysical Journal Letters*, 940, L28
- Polin, A., Nugent, P., & Kasen, D. 2019, *ApJ*, 873, 84
- . 2021, *ApJ*, 906, 65
- Rest, A., Suntzeff, N. B., Olsen, K., et al. 2005, *Nature*, 438, 1132
- Rest, A., Matheson, T., Blondin, S., et al. 2008, *ApJ*, 680, 1137
- Röpke, F. K. 2017, in *Handbook of Supernovae*, ed. A. W. Alsabti & P. Murdin, 1185
- Röpke, F. K., Kromer, M., Seitenzahl, I. R., et al. 2012, *ApJL*, 750, L19
- Ruiter, A. J., & Seitenzahl, I. R. 2025, *A&A Rv*, 33, 1
- Scalzo, R. A., Ruiter, A. J., & Sim, S. A. 2014, *MNRAS*, 445, 2535
- Seitenzahl, I. R., Cescutti, G., Röpke, F. K., Ruiter, A. J., & Pakmor, R. 2013, *A&A*, 559, L5
- Seitenzahl, I. R., Ghavamian, P., Laming, J. M., & Vogt, F. P. A. 2019, *PhRvL*, 123, 041101
- Seitenzahl, I. R., Meakin, C. A., Townsley, D. M., Lamb, D. Q., & Truran, J. W. 2009, *ApJ*, 696, 515
- Seok, J. Y., Koo, B.-C., & Onaka, T. 2013, *ApJ*, 779, 134
- Shen, K. J., & Bildsten, L. 2014, *ApJ*, 785, 61
- Shen, K. J., Blondin, S., Kasen, D., et al. 2021, *ApJL*, 909, L18
- Springel, V. 2010, *MNRAS*, 401, 791
- Taubenberger, S. 2017, in *Handbook of Supernovae*, ed. A. W. Alsabti & P. Murdin, 317
- Tiwari, V., Graur, O., Fisher, R., et al. 2022, *MNRAS*, 515, 3703
- Torres, S., Rebassa-Mansergas, A., Camisassa, M. E., & Raddi, R. 2021, *MNRAS*, 502, 1753
- Truelove, J. K., & McKee, C. F. 1999, *ApJS*, 120, 299
- Vogt, F. P., Álvarez, J. L., Calia, D. B., et al. 2018, *A&A*, 618, L7
- Vogt, F. P. A., Bonaccini Calia, D., Hackenberg, W., et al. 2017, *Phys. Rev. X*, 7, 021044
- Warren, D. C., & Blondin, J. M. 2013, *MNRAS*, 429, 3099
- Warren, J. S., & Hughes, J. P. 2004, *ApJ*, 608, 261
- Weilbacher, P. M., Palsa, R., Streicher, O., et al. 2020, *A&A*, 641, A28
- Wieczorek, M. A., & Meschede, M. 2018, *Geochemistry, Geophysics, Geosystems*, 19, 2574
- Woosley, S. E., & Weaver, T. A. 1994, *ApJ*, 423, 371